



OPEN Synergetic effects of nano-boehmite and Y nano-zeolite on catalytic cracking of residue oil

Ehsan Amini¹✉, Kamran Ahmadi¹, Alimorad Rashidi²✉, Amir Ali Youzbashi¹, Mehran Rezaei³ & Sakineh Mesgar⁴

Boehmite nanoparticles and NaY nanozeolite were synthesized by co-precipitation and hydrothermal methods, respectively, and characterized by XRD, FT-IR, TG-DTA, BET, and SEM techniques. XRD and BET analyses demonstrated the formation of boehmite nanoparticles with a surface area of 350 m²/g and high crystallinity NaY nanozeolite with a surface area of 957 m²/g. In order to evaluate the effect of the content of the mesoporous boehmite nanoparticles on the catalytic performance of the Residue Fluid Catalytic Cracking (RFCC) catalyst, alumina active matrix-based and silica inactive matrix-based catalysts were prepared. Results actually demonstrated that the acidity of the zeolite composition improved with the addition of boehmite nanoparticles. On the other hand, in equal zeolite content, the alumina active matrix-based catalyst possessed higher acidity (NC₃₀B₂₀, 3.44 mmol NH₃/g catalyst) than the silica inactive matrix-based catalyst (NC₃₀B₀, 2.31 mmol NH₃/g catalyst). Microactivity tests (MAT) demonstrated that, with equal zeolite content, active matrix-based catalysts exhibited higher catalytic performance than inactive matrix-based catalyst. Furthermore, the active matrix-based catalyst (NC₃₀B₂₀) with a surface area of 370 m²/g showed the optimum catalytic performance in the RFCC process. The synthesized NC₃₀B₂₀ catalyst with 20 wt% mesoporous boehmite nanoparticles as an active matrix and 30 wt% zeolite nanoparticles balanced with silica had the highest gasoline yield (42 wt%) and gasoline selectivity (65.1 wt%). The catalytic performance test results showed that in equal MAT conversion (almost 64 wt%), the synthesized NC₃₀B₂₀ catalyst had higher catalytic performance than the commercial catalyst.

Keywords Mesoporous, Nanoboehmite, Nanozeolite, RFCC catalyst, Catalytic cracking

Fluid catalytic cracking (FCC) is one of the most important units in oil refineries for the conversion of atmospheric and vacuum residues into valuable products such as gasoline^{1–6}. The catalyst is a more effective aspect of the FCC process since the catalyst performance as well as how the unit is operated determine both the quantity and quality of the products^{2,4}. It's well known that the catalyst acid sites are responsible for cracking heavy hydrocarbon molecules via the carbonium ion mechanism^{2,7–8}. Typically, the RFCC catalyst is composed of four major components, such as zeolite, matrix, filler, and binder. Among them, HY zeolite with a faujasite framework is the key component that provides much of the catalytic activity and product selectivity^{2,9–12}. In fact, the RFCC catalyst's performance largely depends on the quality and quantity of the zeolite particles. Highly ordered crystalline structure and acidity are the unique properties of zeolites that are responsible for heavy hydrocarbon molecules cracking into lighter ones^{13–16}. The commercial RFCC catalysts are composed of HY zeolite particles with about 1–2 μm diameter that are dispersed in an amorphous matrix^{2,10}.

The HY zeolite with faujasite framework is composed of a uniform microporous structure, in which oxygen rings restrict the 7.4 Å, opening connecting supercages with a 12 Å diameter^{17–20}. These uniform pore structures provide acidic active sites on the internal as well as the external surfaces of the zeolite crystallites, with the major ones being placed within the zeolite pores^{21,22}. So, as a result of limitations related to pore size, the catalytic properties of zeolite are limited to reactant molecules with diameters lower than zeolite pore size²³. The critical diameter of residue or heavy oil hydrocarbon molecules with a boiling point of > 400 °C is from 1.2 to 15 nm⁴. These large molecules cannot penetrate zeolite micropores and must be cracked on the external surface of zeolite and the mesoporous acidic sites of the active matrix^{24–31}. Hence, in order to fulfill the above-mentioned

¹Research Department of Semiconductors, Material and Energy Research Center, Karaj, Iran. ²Nanotechnology Research Center, Research Institute of Petroleum Industry, Tehran, Iran. ³School of Chemical, Petroleum and Gas Engineering, Iran University of Science and Technology, Tehran, Iran. ⁴Department of Organic Chemistry, Faculty of Chemistry, University of Mazandaran, Babolsar, Iran. ✉email: amini.tares@gmail.com; rashidiam@ripi.ir

requirement, mesoporous alumina nanoparticles as an active matrix and nanozeolite particles can be effectively utilized. With the reduction of zeolite particle size from micrometer to nanometer, the ratio of external to internal surface area strongly increases^{26,32,33}. Therefore, zeolite nanoparticles have a larger external surface area and higher surface activity than zeolite microparticles^{34–36}.

Unlike inactive matrix, which does not have enough acidity to influence the catalyst performance, active matrix can influence the catalyst performance, but it has a lower impact on the catalytic performance compared to zeolitic compounds^{37–39}. Among the different alumina components, boehmite is one of the most important components used in catalyst formulations⁴⁰. The mesoporous structure of boehmite, which can be preserved after calcination, as well as its sufficient acidity for pre-cracking heavy hydrocarbon molecules, are the most important reasons for its use as an RFCC catalyst matrix^{41,42}. In fact, the large hydrocarbon molecules pre-crack on the alumina active matrix into intermediate molecules. Then these intermediate molecules penetrate into the zeolite micropores and crack further into the valuable products⁴³.

The use of heavier feedstocks by RFCC units and their conversion to valuable products is growing year by year. It's well known that the catalytic cracking of these heavy feedstocks will be diffusion-limited^{24,25,44,45}. Therefore, in order to decrease the diffusion resistance of large hydrocarbon molecules in catalyst pores, one has to increase the external surface area of zeolite by reducing the particle size as well as providing a mesoporous active site in the catalyst matrix structure^{26,46,47}. In fact, using mesoporous boehmite nanoparticles as an active matrix and Y nanozeolite in the RFCC catalyst formulation can fulfill this limitation^{26,31–39}. Therefore, the study of the synergetic effect of mesoporous alumina and HY zeolite nanoparticles in the structure of RFCC catalysts and the examination of their catalytic performance are highly favorable.

There have been several studies on the effect of the RFCC catalyst matrix on catalytic performance, but most of them usually used model feedstocks, e.g., 1,3,5-Triisopropylbenzene, Cumene, etc. These types of processes can only provide a general recommendation on the catalyst's potential. Since the performance of RFCC catalysts is affected by various parameters, such as feedstock characteristics, test equipment, and operating parameters, it is necessary to evaluate the performance of the prepared catalysts against a real RFCC unit feedstock.

The effects of HY zeolite particle size and content on the catalytic performance of RFCC catalysts were evaluated in our previous work⁴⁸. In order to achieve this objective, a series of catalysts were prepared using a silica inactive matrix, and the impact of zeolite on the catalytic performance was evaluated. The results indicated that the catalyst with 30 wt% HY nanozeolite dispersed in a silica inactive matrix exhibited the highest gasoline yield and gasoline selectivity.

So, in this work, in order to investigate the effect of the mesoporous active matrix on RFCC catalyst performance, a series of RFCC catalysts based on mesoporous boehmite and HY zeolite nanoparticles were prepared.

The synergetic effects of mesoporous alumina matrix and HY zeolite nanoparticles on the RFCC catalytic performance under ASTM conditions and using a real feedstock were studied. Ultimately, the optimized synthesized catalyst was compared to the commercial one.

Experimental

Synthesis of mesoporous boehmite nanoparticles

750 ml of deionized water was added to a precipitation reactor and heated to 57 °C. Then, 306 ml of sodium aluminate solution (1 mol/L) was fed to the precipitation reactor with a feed flow rate of 18 ml/min. Also, the appropriate amount of aluminum sulfate solution (0.5 mol/L) was introduced into the precipitation reactor. The flow rate of the aluminum sulfate solution was controlled in order to keep the pH of the mixed solution at 9.0. The temperature of both sodium aluminate and aluminum sulfate solutions was adjusted to 57 °C, and after the precipitation process, the suspension was aged at 57 °C for 1 h under vigorous stirring. After that, the precipitate was separated by centrifuging, washed three times with deionized water, and finally dried at 120 °C for 24 h⁴⁹.

Synthesis of nanozeolite

In our previous work, a hydrothermal method was used to synthesize the NaY nanozeolite⁴⁸. In a typical synthesis, a quantity of 5.5 g of pseudo-boehmite were initially added to a solution consisting of 52.6 g of tetramethylammonium hydroxide (TMAOH: 25 wt%) and an appropriate quantity of deionized water in a 200-ml propylene bottle. Following a night of stirring, 8.3 g of tetramethylammonium bromide (TMABr, ≥ 98%) were added and vigorously stirred for 5 h. Subsequently, 23 g of sodium silicate solution (Merck, extra pure, 7.5–8.5 wt% Na₂O, 25.5–28.5 wt% SiO₂) were added during the stirring process. After 3 days of vigorous stirring at room temperature, the resulting mixture was transferred to an autoclave, where it was sealed tightly and kept for 6 days at 100 °C without stirring. After centrifugation, the precipitate was washed three times with deionized water, then dried at 80 °C for 24 h.

Synthesis of RFCC catalysts

The RFCC catalysts were synthesized using different amounts of boehmite nanoparticles and a constant quantity of 30 wt% HY nanozeolite as an active component. In a typical synthesis, firstly, the ion exchange procedure utilizing ammonium sulfate was performed four times in order to transform the synthesized NaY nanozeolite into HY zeolite, which is applicable for RFCC catalysts. A specified quantity of boehmite nanoparticles and HY nanozeolite were then added to an appropriate quantity of colloidal silica at ambient temperature. After that, the mixture was stirred and a gel was formed. The gel was aged at room temperature for 1 h, dried at 80 °C for 24 h, and then calcined at 600 °C with a ramp rate of 3 °C/min for 5 h in an air atmosphere. The nominal content of boehmite nanoparticles was 10, 20, and 30 wt%, respectively, while the constant content of HY nanozeolite was 30 wt% in the final composition of prepared catalysts. The corresponding catalysts were identified as NC₃₀B₁₀, NC₃₀B₂₀, and NC₃₀B₃₀, respectively. The synthesized catalyst without boehmite was also designated as NC₃₀B₀.

Characterization

A PANalytical X'Pert-Pro X-ray diffractometer, which was equipped with a Cu-K α monochromatized radiation source and a Ni filter, was utilized for the X-ray diffraction (XRD) analysis. A SPECTRUM 2 (PerkinElmer) Fourier transform infrared (FTIR) spectrophotometer was used to record the infrared spectra. A Netzsch STA 409 model system with a heating rate of 10 °C/min in a static air atmosphere was used to perform thermogravimetric (TG) and differential thermal analysis (DTA).

An automated gas adsorption analyzer (ASAP 2020, Micromeritics) was used to perform the nitrogen adsorption/desorption analysis (BET) at -196 °C. A VEGA@TESCAN instrument was used to obtain the scanning electron microscope (SEM) images. A Micromeritics Chemisorb 2900 apparatus was used to determine the acidity of the catalysts by NH₃-TPD analysis. Typically, 0.1–0.3 g of catalyst were loaded into a quartz U-tube reactor. Prior to conducting the analysis, the catalyst was degassed under the He atmosphere at 400 °C for a duration of 2 h. The catalyst was then exposed to a mixture of NH₃ and the He stream for a duration of 1 h at 50 °C, followed by a purge by the He stream for a duration of 30 min. Following this, the samples were heated to 750 °C at a ramp rate of 10 °C/min in the He stream. The quantity of NH₃ desorbed was then measured using a thermal conductivity detector (TCD).

Catalytic performance evaluation

A fixed-bed microactivity test (MAT) unit conforming to ASTM D5154 was used to conduct catalytic activity and selectivity tests for residue fluid catalytic cracking. According to this standard, the products from the MAT unit were classified as gas products (i.e., H₂, H₂S, dry gas C₁-C₂, and LPG C₃-C₄, etc.), gasoline products defined to have a boiling point range of >C5 up to 216 °C, light cycle oil (LCO) products defined to have a boiling point range of 216 to 343 °C, heavy cycle oil (HCO) products defined to have a minimum boiling point of 343 °C, and coke.

The test method apparatus is shown in Scheme 1. The unit was equipped with a collection system for both liquid and gas products. The volume of the collected gas products was determined by displacement of a saturated NaCl solution. Actually, the volume of the displaced solution provided a quantitative measurement of the volume of gas collected. The composition of the collected gas products was determined by a gas chromatograph (Clarus 580 GC, PerkinElmer) equipped with thermal conductivity (TCD) and flame ionization (FID) detectors. Therefore, by determining the volume and composition of the collected gas, the weight of the gas products was calculated.

A simulated distillation gas chromatograph (Clarus 580 GC, PerkinElmer) equipped with a flame ionization detector was used to determine the boiling point range of liquid products.

The coke content of the spent catalysts was quantified by passing an oxygen-containing stream (100 ml/min., 5.0 vol% O₂ in N₂) over a certain amount (0.2 g) of the spent catalysts at an elevated temperature (5 °C/min., RT to 900 °C) and determining the amounts of CO and CO₂ formed by GC. Also, coke content was calculated by weight loss during the oxidation process.

The catalytic activity tests were carried out in the MAT unit at 482 °C with a weight hourly space velocity (WHSV) of 16 h⁻¹. Before the catalytic tests all catalysts were steamed with 80% water vapor in N₂ at 800 °C for 15 h. As MAT results, the conversion, yield, and selectivity of products (gas, gasoline, LCO, HCO, and coke) were determined. The RFCC unit feedstock from Arak Oil Refinery Company was utilized in for all MAT tests. The specifications of the Arak Oil Refinery Company's RFCC feedstock are presented in Table 1.

The MAT conversion was calculated as the difference between the weight of feed used and the weight of unconverted material divided by the weight of feed used times 100%. According to ASTM D5154 definitions, unconverted material was defined as all liquid products with a boiling point above 216 °C (i.e., LCO + HCO). So, the conversion was calculated using the simplified Eq. (1).

$$\text{Conversion, wt.}\% : 100\% - (\text{HCO Yield, wt.}\% + \text{LCO Yield, wt.}\%) \quad (1)$$

The product yield of the *i*th product was calculated as one hundred times the weight of the *i*th product (W_i) divided by the weight of feed used (W_F), as in Eq. (2):

$$Y_i, \text{ wt.}\% : (W_i/W_F) \times 100\% \quad (2)$$

The gasoline selectivity was calculated using the Eq. (3).

$$\text{Gasoline Selectivity} : (\text{Gasoline Yield, wt.}\% / \text{Conversion, wt.}\%) \times 100 \quad (3)$$

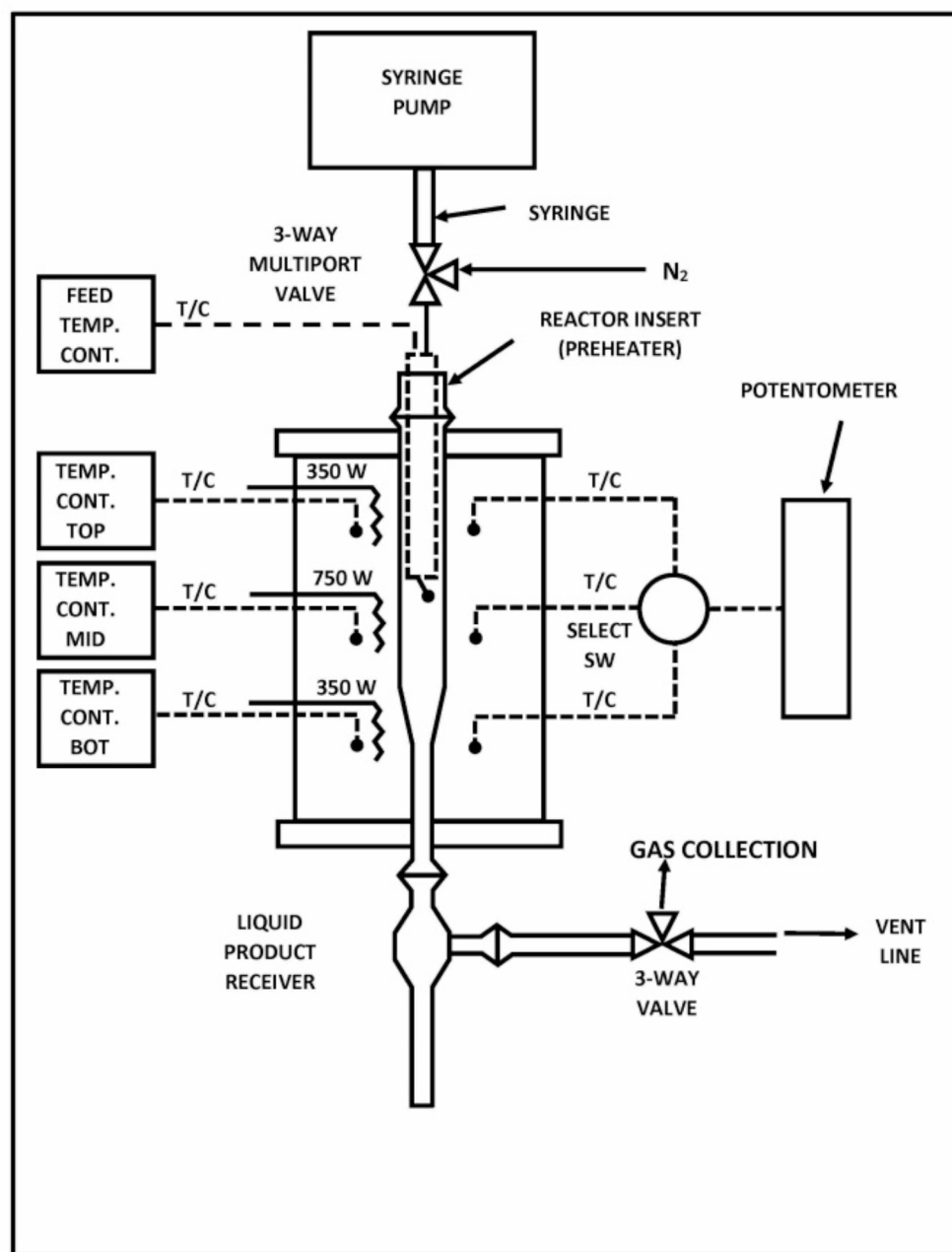
Results and discussion

Synthesis of mesoporous boehmite nanoparticles

Figure 1 shows the X-ray diffraction pattern of the synthesized boehmite nanoparticles. As compared with the reference pattern (Boehmite, 00-005-0190), the synthesized boehmite powders present the diffraction characteristic of the boehmite structure with the orthorhombic crystalline system. As can be seen, the broad peaks of the XRD pattern indicate the formation of nanobohmite powder. The characteristic diffraction peaks for boehmite appear at 14.38°, 28.11°, 38.41°, 49.05°, 64.03°, and 71.91° (2 θ), which are related to the (020), (021), (130), (150), (132), and (152) planes in the orthorhombic crystalline system, respectively.

The average crystallite size of the synthesized boehmite nanoparticles was calculated from the half-width of the main diffraction peaks using the Scherer formula, and the obtained results are presented in Table 2.

Figure 2 shows the FTIR spectrum of the synthesized boehmite nanoparticles. Two broad bands in the FTIR spectrum of the synthesized boehmite can be seen at 3050–3100 cm⁻¹ and 3200–3300 cm⁻¹, which are related to



Scheme 1. Microactivity Test (MAT) system.

the stretching vibrations of hydroxyl groups. Moreover, the peak at $1500\text{--}1600\text{ cm}^{-1}$ is attributed to the adsorbed water. Two peaks at $1050\text{--}1100\text{ cm}^{-1}$ and $1100\text{--}1200\text{ cm}^{-1}$ are associated with bending vibrations of Al-OH. Three peaks in the region of $450\text{--}750\text{ cm}^{-1}$ are attributed to the metal-oxygen's (Al-O) bending and stretching vibration⁵⁰.

Figure 3 shows the TG- DTA curves of the synthesized boehmite nanoparticles. The TG curve shows the weight loss (approximately 15 wt%) in the region of $\sim 50\text{--}150\text{ }^{\circ}\text{C}$, corresponding to a broad endothermic peak at the same region in the DTA curve. This weight loss and the endothermic peak are related to the evaporation of the surface adsorbed water and the water trapped in pores. With increasing temperature, a weight loss of about 15 wt% in the region of $\sim 300\text{--}500\text{ }^{\circ}\text{C}$ is found, which corresponds to a broad endothermic peak at the same region in the DTA curve, which is attributed to the crystallization of metal hydroxide into metal oxide and the removal of residual hydroxide groups. In fact, this was attributed to the phase transformation from AlOOH to $\gamma\text{-Al}_2\text{O}_3$ ⁵⁰.

In order to study the specific surface area and pore structure of the synthesized boehmite nanoparticles, the BET/BJH analysis was performed. According to the results in Table 2, the synthesized sample shows a BET

Item	Measured values	Test Method
Specific gravity (15.6 °C/15.6 °C)	0.9401	ASTM D792
Total Sulfur (wt%)	1.01	ASTM D4294
Total Nitrogen (ppm)	1976	ASTM D4629
Conradson Carbon (wt%)	4.45	ASTM D189
Ni (ppm)	5.9	UOP391
V (ppm)	8.7	UOP391
Distillation (°C)		ASTM D1160
IBP	225	
10 vol%	365	
30 vol%	477	
50 vol%	489	
70 vol%	507	
90 vol%	521	
FBP	534	

Table 1. Specification of Arak Oil Refinery Company RFCC feedstock.

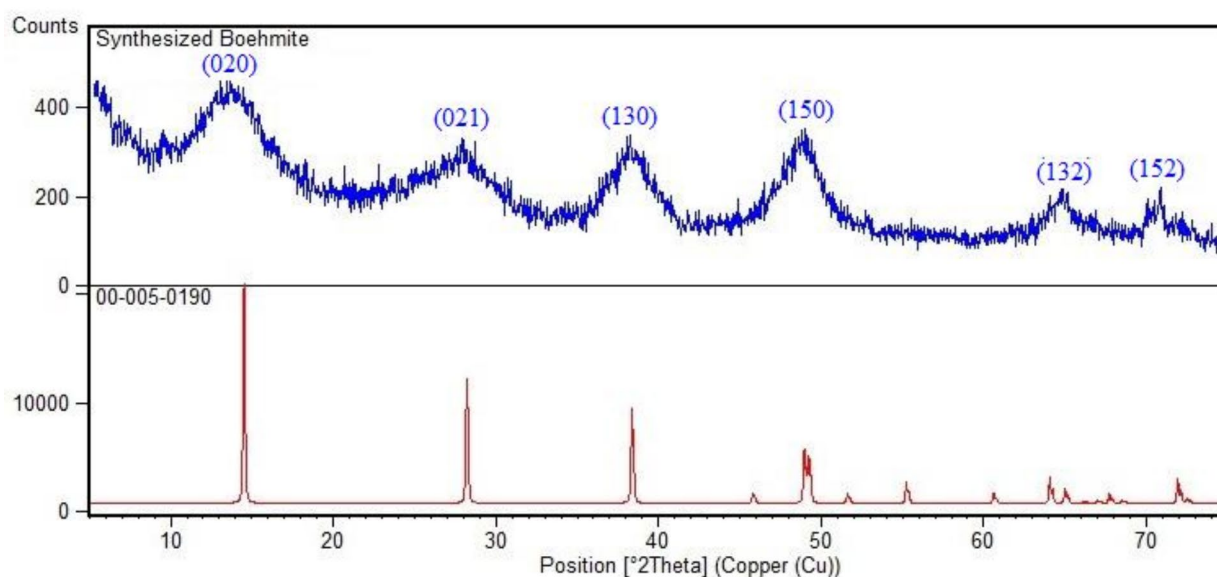


Fig. 1. X-ray diffraction pattern of the synthesized boehmite nanoparticles and reference pattern (Boehmite, 00-005-0190).

Sample	Average crystallite size (nm)	Surface area (m ² /g)	Pore volume (cm ³ /g)	Average Pore size (nm)
Boehmite nanoparticles	6	350	0.61	7.1
Y zeolite nanoparticles	33	957	0.35	1.13

Table 2. Structural properties of the synthesized boehmite and Y zeolite nanoparticles.

surface area of 350 m²/g with a pore volume of 0.61 cm³/g. Moreover, the average pore size of the synthesized sample is 7.1 nm. Figure 4 shows the N₂ adsorption/desorption isotherm and pore size distribution curve of the prepared sample. According to the IUPAC classification, the N₂ isotherm is type IV with an H2-type hysteresis loop. This type of hysteresis is usually found in solids consisting of particles crossed by partially cylindrical channels or made by agglomerates or aggregates of spheroidal particles with non-uniform size and/or shape pores⁵⁴. The pore size distribution curve of the prepared sample is shown in Fig. 4b. The synthesized boehmite shows a pore size in the mesopore region, which is suitable for the preparation of the RFCC catalyst.

The SEM images of the synthesized boehmite nanoparticles with different magnifications are shown in Fig. 5. As can be seen, the SEM images clearly demonstrate that the structure has a spherical shape. The particle size of

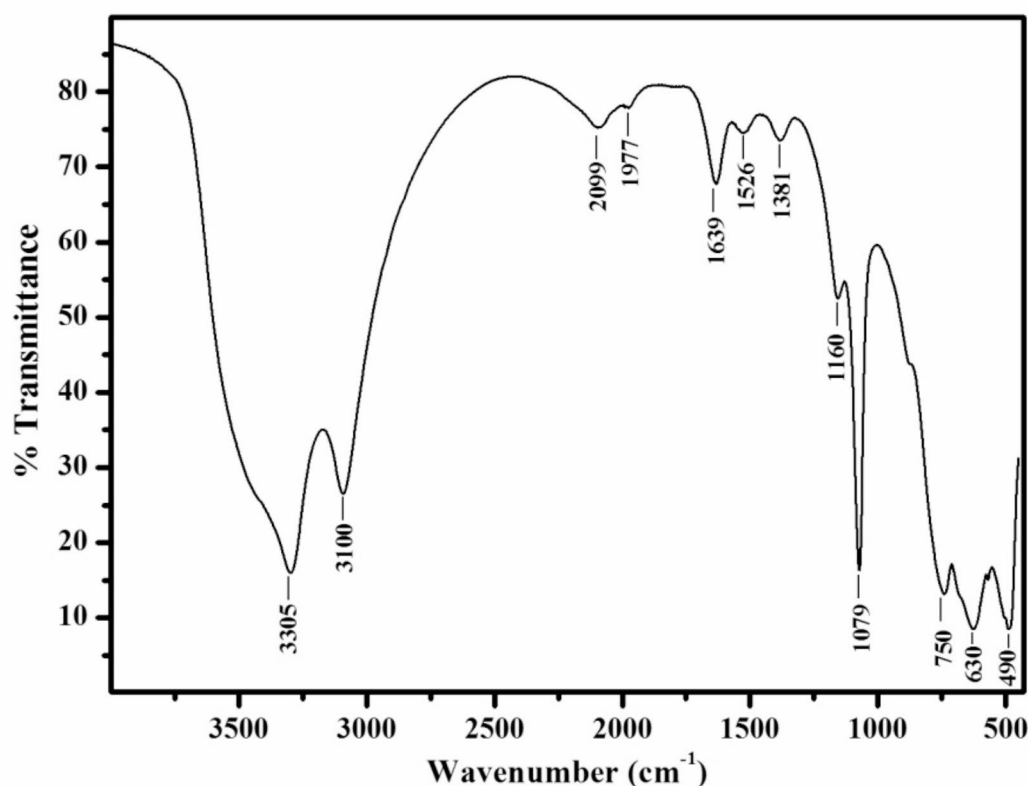


Fig. 2. FT-IR spectrum of the synthesized boehmite nanoparticles.

the synthesized boehmite nanoparticles was uniform, ranging from 20 to 40 nm. However, these particles were physically attached and formed uniform spheres.

Synthesis of nanozeolite

The X-ray diffraction pattern of the synthesized NaY nanozeolite powder is shown in Fig. 6. As compared with the reference pattern (Faujasite, 00-039-1380), the synthesized nanozeolite powder presents the diffraction pattern characteristic of a faujasite structure with a cubic crystalline system. The sharp peaks in the XRD pattern indicate the formation of zeolite powder with high crystallinity.

The average crystallite size of the synthesized NaY nanozeolite was also calculated from the half-width of the main diffraction peaks using the Scherer formula, and the results are presented in Table 2.

The FT-IR spectrum of the synthesized NaY nanozeolite is displayed in Fig. 7. A wide band at 3460 cm^{-1} was due to the stretching vibration of structural hydroxyl groups and water molecules. Also, the peak at 1640 cm^{-1} was due to the bending vibration of water molecules. The bands in the region of 1200 and 900 cm^{-1} were ascribed to the internal tetrahedral and external linkage asymmetrical stretching vibrations, respectively. Furthermore, the bands at 725 and 790 cm^{-1} were attributed to internal tetrahedral and external linkage symmetrical stretching vibrations, respectively⁵¹. The band at around 577 cm^{-1} was related to the structural vibration of the double ring (D6R) units, which is a special characteristic of the Y zeolite structure^{52,53}. In fact, this band demonstrated the formation of a zeolitic structure. Likewise, the band at 465 cm^{-1} was related to the metal-oxygen bonding vibration at tetragonal holes TO_4 ($\text{T} = \text{Si}$ or Al) in the zeolite structure²⁸.

The N_2 adsorption/desorption isotherm and pore size distribution of the synthesized NaY nanozeolite are shown in Fig. 8. According to the IUPAC classification, the N_2 isotherm is type I, which is related to microporous materials⁴⁴. As can be seen, the isotherm shows an intensive rise in N_2 adsorption at very low relative pressure (P/P^0) and then a flat curve at higher relative pressure, which is a special characteristic of microporous materials. The structural properties of the prepared sample are reported in Table 2. According to the results in Table 2, the specific surface area is $957\text{ m}^2/\text{g}$, and the external surface area based on the t-plot calculation is $102\text{ m}^2/\text{g}$ for the synthesized NaY nanozeolite. According to the N_2 isotherm and BET result, the pore size of the synthesized zeolite is in the micropore range ($< 2\text{ nm}$), which is in agreement with the pore size distribution (Fig. 8b).

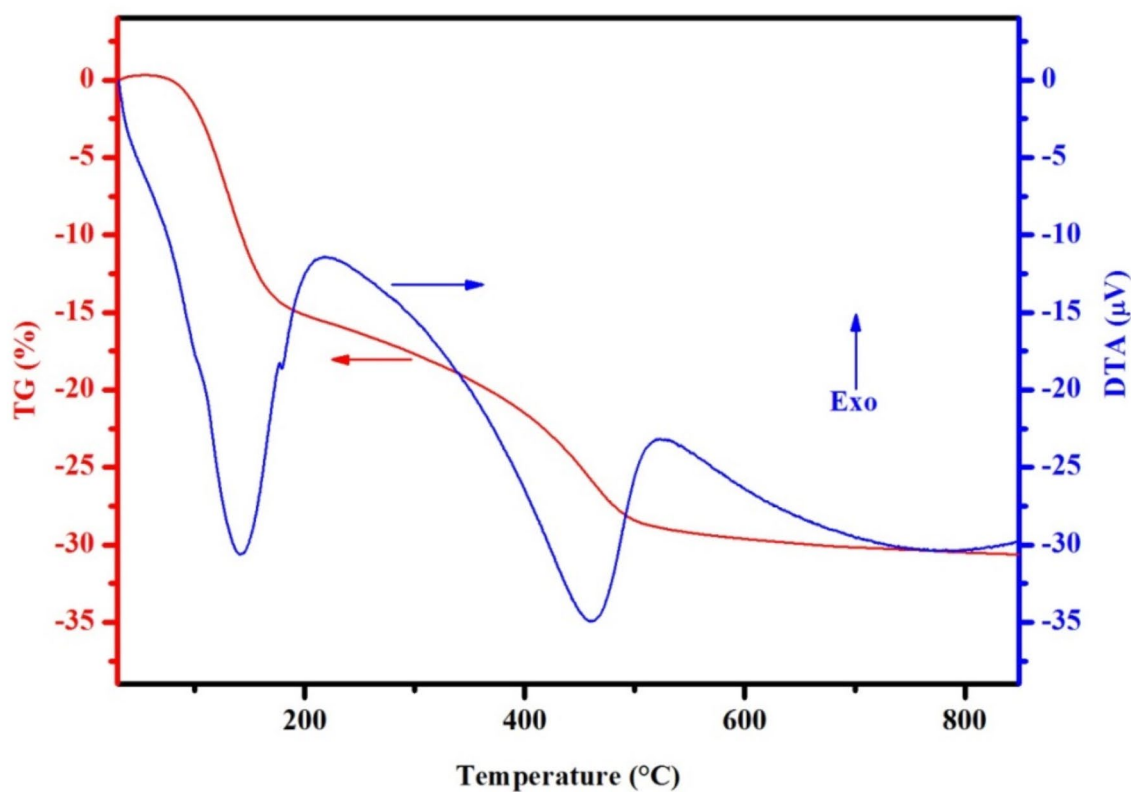


Fig. 3. TG-DTA diagram of the synthesized boehmite nanoparticles.

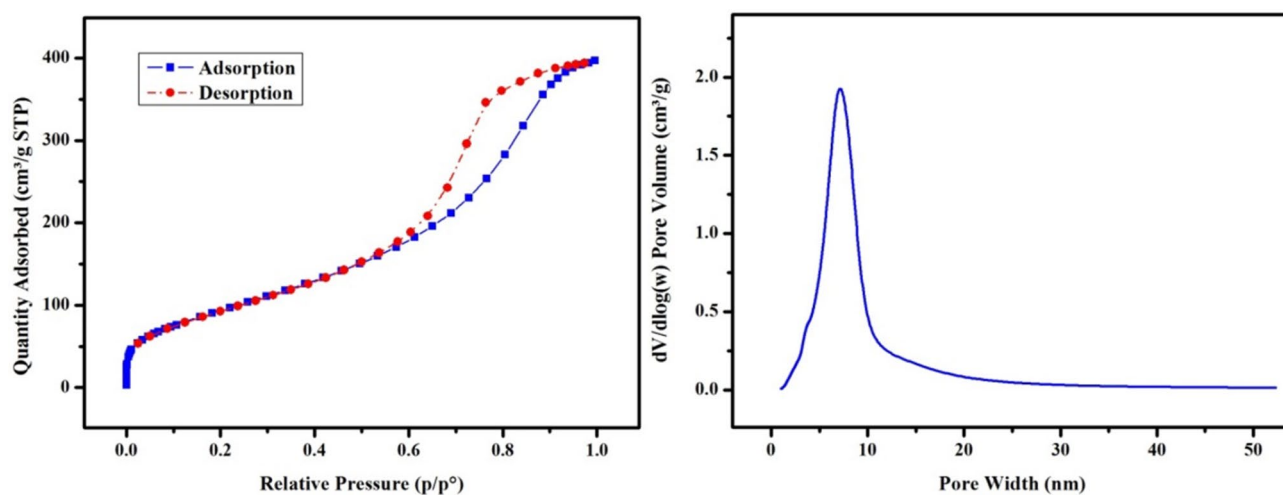


Fig. 4. N_2 adsorption/desorption isotherm (a) and pore size distribution (b) of the synthesized boehmite nanoparticles.

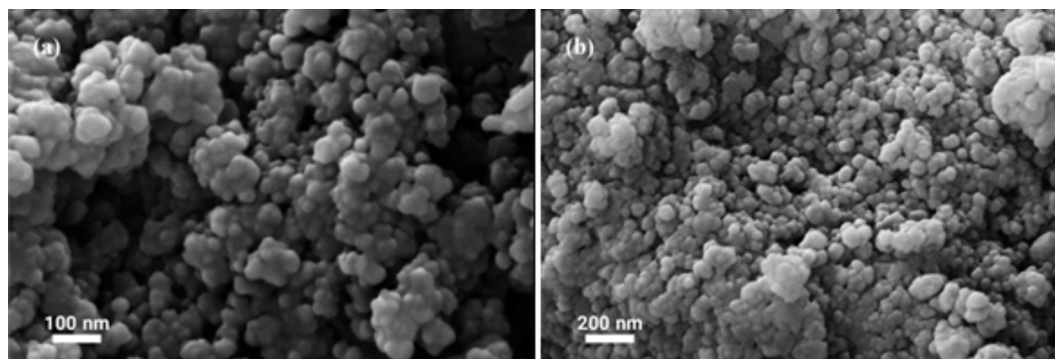


Fig. 5. SEM images of the synthesized boehmite nanoparticles with different magnifications.

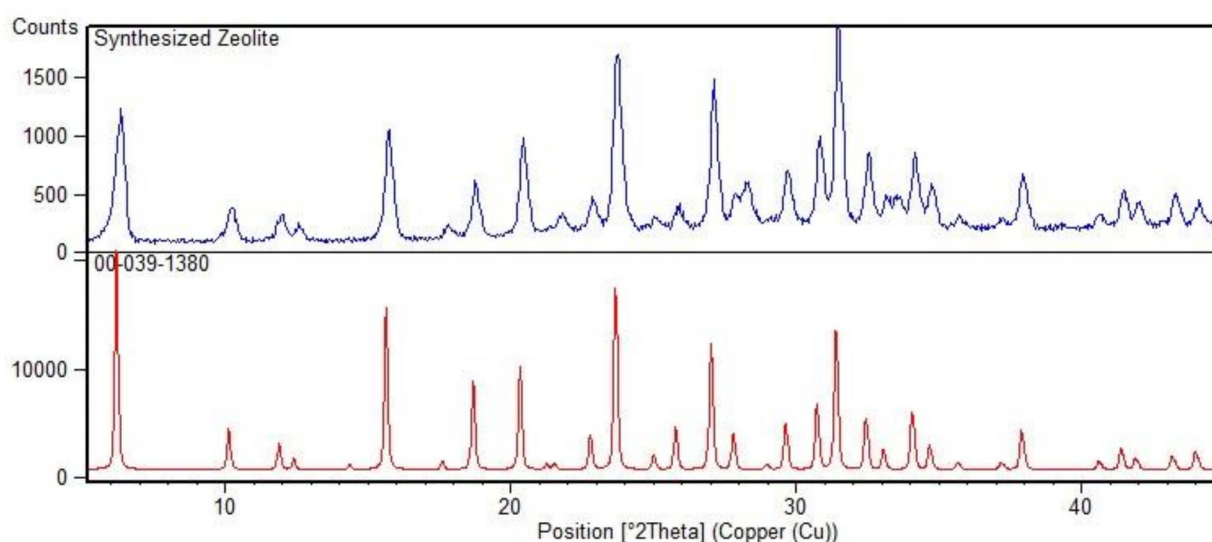


Fig. 6. X-ray diffraction pattern of the synthesized NaY nanozeolite and reference pattern (Faujasite, 00-039-1380).

Figure 9 shows the SEM images of the synthesized NaY nanozeolite. According to the SEM images, particles with cubic shapes are clearly formed. The particle size distribution of the synthesized NaY nanozeolite was uniform, ranging from 20 to 30 nm.

Synthesis of RFCC catalysts

The X-ray diffraction patterns of the prepared catalysts with different boehmite contents are shown in Fig. 10. It clearly demonstrates the presence of a Y zeolite structure in the prepared catalysts. The broad diffraction peak that appeared at $2\theta = 15\text{--}30^\circ$ is related to the amorphous silica matrix.

The acidity of the catalysts was studied by NH_3 temperature-programmed desorption (NH_3 -TPD) analysis. The acidic site distribution and the total acidity of the catalysts can be obtained from the peak position, shape, and area of the desorption peaks, respectively. Figure 11 illustrates the NH_3 -TPD curves of the prepared catalysts without boehmite (NC_{30}B_0) and with 20 wt% boehmite ($\text{NC}_{30}\text{B}_{20}$). As can be seen, the curves show two main desorption peaks. The low-temperature peak can be related to the desorption of NH_3 from weak acid sites or non-acidic sites, weak Bronsted acid sites, Lewis acid sites, silanol groups, and the formation of NH_4^+ (NH_3) $_n$ ($n \geq 1$) groups^{55,56}. The high-temperature peak can be attributed to the desorption of NH_3 from strong Bronsted and Lewis acid sites^{57–59}. As can be seen, the acidity of the prepared catalysts increased with the addition of boehmite nanoparticles as an active matrix to the catalyst composition. On the other hand, in equal zeolite content (30 wt%), the catalyst with the active matrix ($\text{NC}_{30}\text{B}_{20}$) has higher acidity than the catalyst with the inactive matrix (NC_{30}B_0). In fact, this higher acidity of the active matrix-based catalyst is related to the acidic sites of the mesoporous alumina matrix that have a key role in the precracking of heavy hydrocarbon molecules that cannot enter the zeolite micropore.

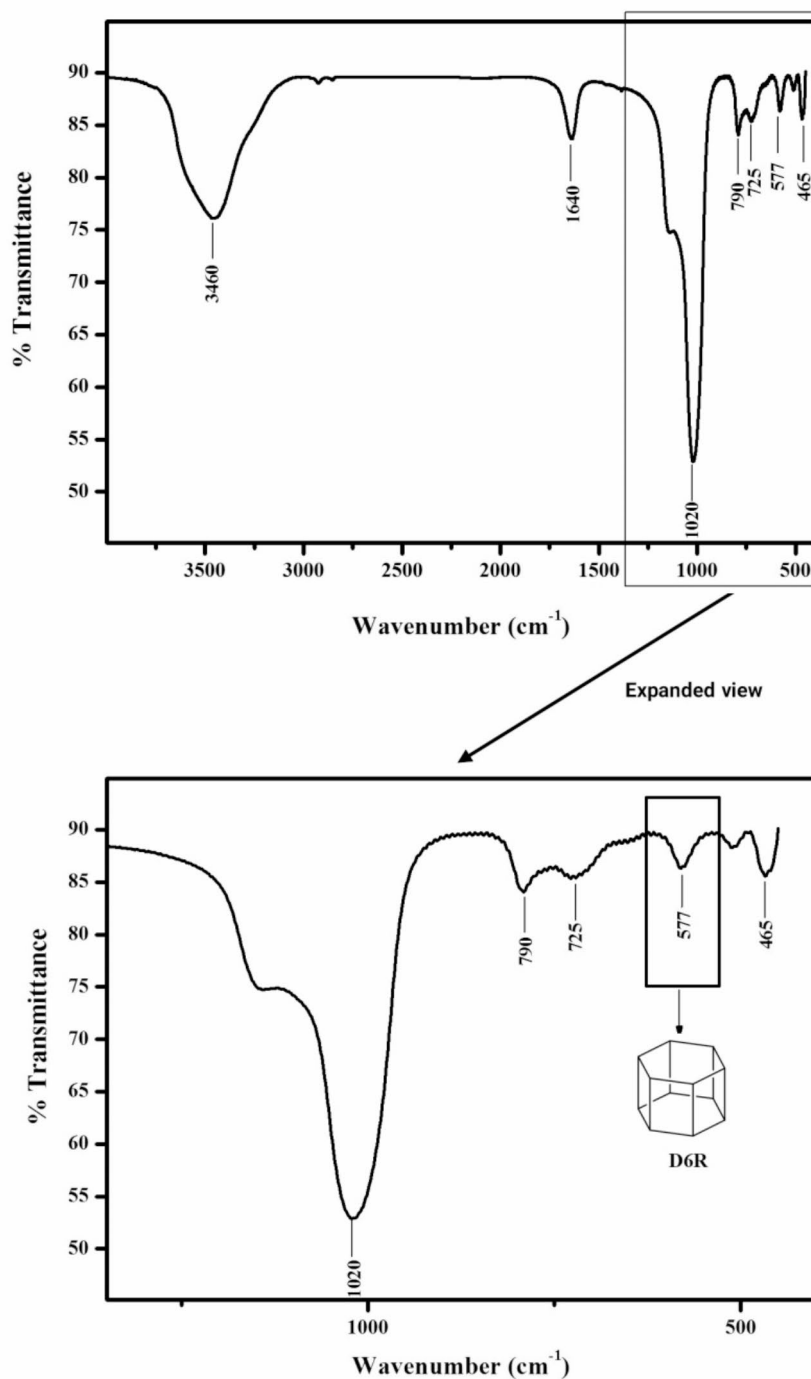


Fig. 7. FT-IR spectrum of the synthesized NaY nanozeolite.

Figure 12a shows the N₂ adsorption and desorption isotherms of the catalysts prepared with different boehmite contents. According to the IUPAC classification, the N₂ isotherms are type IV with an H2-type hysteresis loop. This type of hysteresis is usually found on solids consisting of particles crossed by partially cylindrical channels or made by agglomerates or aggregates of spheroidal particles with a non-uniform size and/or shape pores⁵³. As can be seen, with the addition of boehmite nanoparticles to the catalyst composition, the adsorption of N₂ molecules in the saturated pressure ($P/P^0 = 1$) decreased, which is attributed to the decrease in the pore volume of the catalyst. The pore size distribution curves of the prepared catalysts are shown in Fig. 12b. Based on this

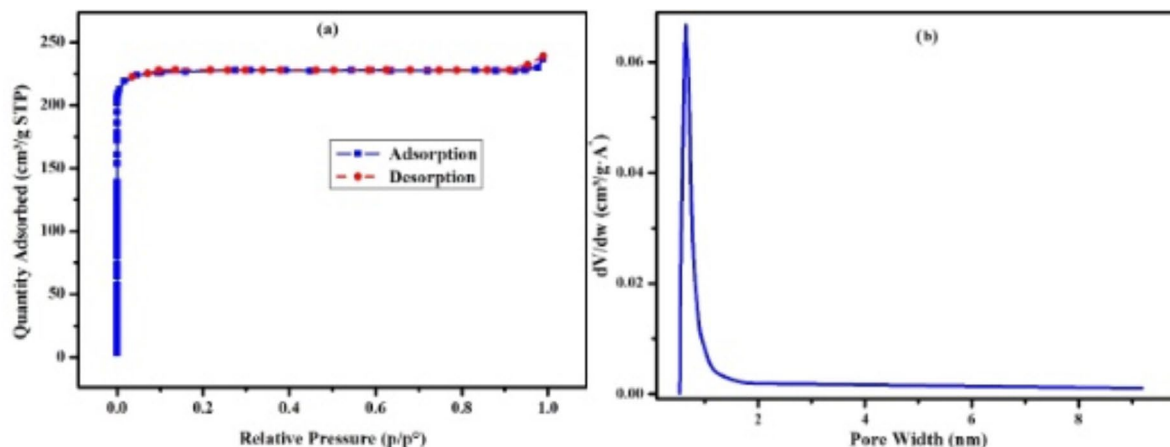


Fig. 8. N_2 adsorption/desorption isotherm (a) and pore size distribution (b) of the synthesized NaY nanozeolite.

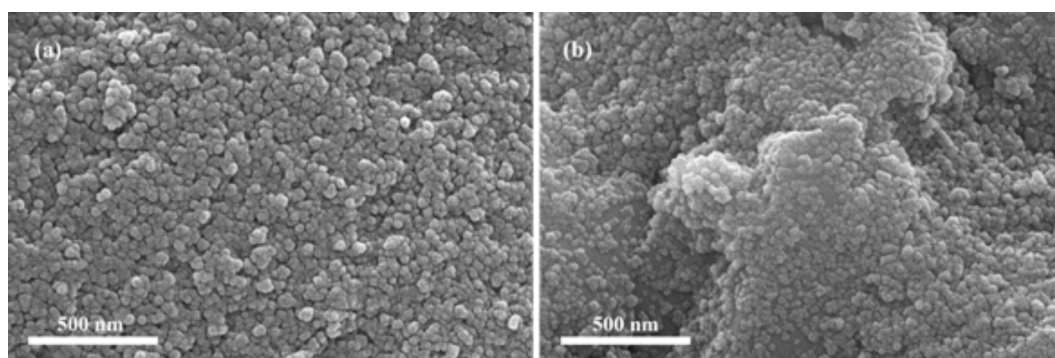


Fig. 9. SEM images of the synthesized NaY nanozeolite with different magnifications.

figure, all catalysts have a pore size in the mesopore and micropore regions. The structural properties of the prepared catalysts are presented in Table 3. Here, the BET analysis demonstrated that the addition of boehmite nanoparticles to the catalyst composition increased the surface area of all prepared samples. In fact, with the addition of boehmite nanoparticles to the catalyst composition, the pore volume of the prepared catalysts decreased. Still, due to the decrease in pore size, the surface area of the catalysts increased.

The SEM images of the $NC_{30}B_0$ and $NC_{30}B_{20}$ catalysts are presented in Fig. 13. It can be observed that the zeolite and boehmite nanoparticles are well dispersed and incorporated into a silica matrix. However, these particles were physically attached and formed uniform spheres.

Catalytic performance

The modern RFCC catalyst is a composite that consists of different components such as zeolite, matrix, binder, and different additives as promoters. Among them, the active matrix plays a key role in the precracking of heavy hydrocarbon molecules that cannot enter the zeolite micropore. The cracking of model feedstock over synthesized RFCC catalyst has been reported by several authors^{10,59,60}. This type of process can provide a general suggestion of the potential of the catalysts. However, it is necessary to evaluate the performance of the catalysts with real RFCC unit feedstock; hence, in order to evaluate the synergetic effect of mesoporous boehmite nanoparticles as active matrix and zeolite nanoparticles on the catalytic performance of the RFCC catalyst, the cracking reaction was carried out using the RFCC unit feedstock of Arak Oil Refinery Company over the prepared catalysts. In a commercial RFCC catalyst, matrix components are active and crack large hydrocarbon molecules into lighter ones. Therefore, in this work, we prepared catalysts using mesoporous boehmite nanoparticles as an active matrix and zeolite nanoparticles in order to evaluate the synergetic effect of matrix activity and zeolite nanoparticles on the catalytic performance. Figure 14a shows the correlation of MAT conversion with the boehmite content of different prepared catalysts. As can be seen, the MAT conversion increased with the boehmite content. In general, increasing the boehmite content as an active matrix increased the acidity and cracking of hydrocarbon molecules, so the conversion increased. However, boehmite nanoparticles as an active matrix with mesoporous active sites cause the precracking of heavy hydrocarbon molecules to lighter ones. These light hydrocarbons can later enter zeolite micropores and crack into valuable products^{37–39}. On the other hand, with equal nanozeolite

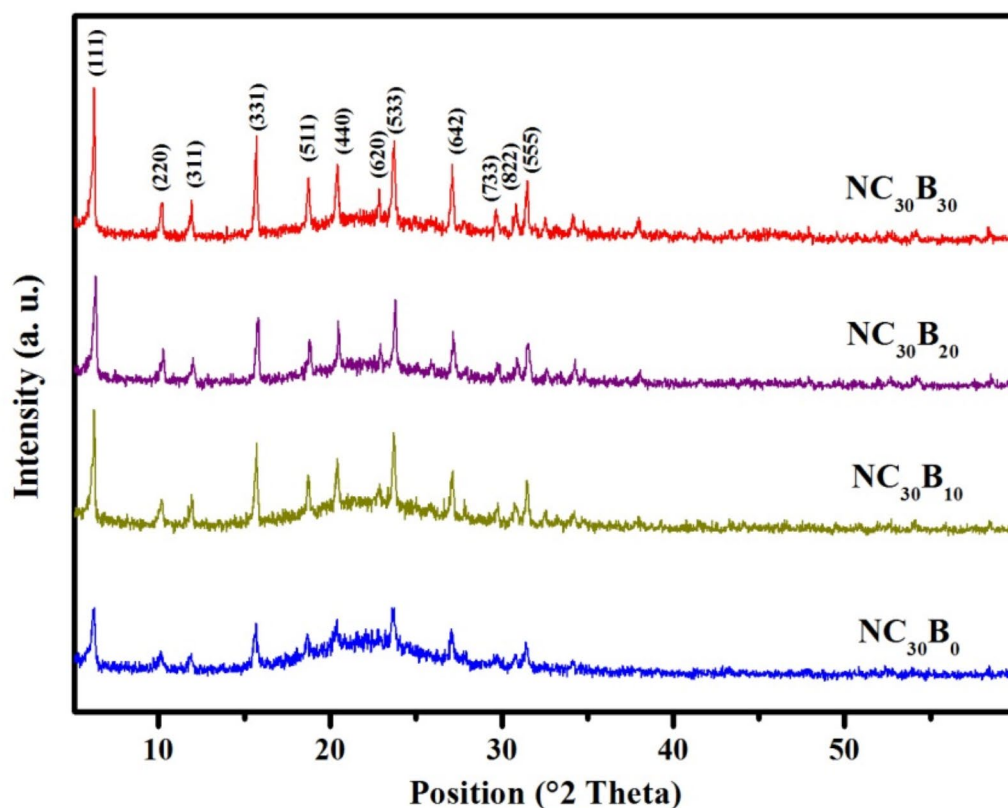


Fig. 10. The X-ray diffraction patterns of the prepared catalysts.

content, the catalysts with the alumina matrix have higher cracking activity than the catalysts with the inactive matrix. In fact, this higher activity of active matrix-based catalysts is related to the mesoporous active site of the alumina matrix, which causes lower molecular diffusion resistance and higher heavy hydrocarbon molecular accessibility.

Figure 14b illustrates the relationship between the product yield and the boehmite content of different prepared catalysts. The gaseous products include dry gas (C_1 - C_2 molecules and other molecules containing H_2 , H_2S , CO , CO_2 , etc.) and LPG (C_3 - C_4). Dry gas is an undesirable product, while LPG is a valuable product. The obtained results revealed that the gas yield increased with the boehmite content. As it is well known, gaseous products are caused by the thermal cracking and overcracking of hydrocarbon molecules on the catalyst acid sites. In fact, the rise in catalyst boehmite content increased the available catalyst acid sites and catalyst conversion, hence the increase in gas yield.

Gasoline is one of the most important products of the RFCC unit. It can be observed that increasing the content of boehmite up to 20 wt% increased the gasoline yield, and a further increase in its content had a negative influence and decreased the gasoline yield. In general, the mesoporous active site in the matrix structure of the catalyst for precracking heavy hydrocarbons that cannot enter zeolite micropores increased with an increase in the content of boehmite in the catalyst. After that, this precracked hydrocarbon entered into zeolite micropores and selectively cracked into a lighter product; hence, gasoline yield increased. In fact, mesoporous acidic sites in alumina structures precrack heavy hydrocarbon molecules, increase the accessibility of these cracked molecules to the active site of zeolite, and cause lower molecular diffusion resistance, but do not result in any blockage of zeolite micropores with heavy hydrocarbon molecules. So, the gasoline yield with selective and controlled cracking increases. As the boehmite content of the catalyst reaches a critical amount, the gasoline yield reaches a steady state and eventually decreases with the further increase of the boehmite content. In fact, further increases in boehmite content intensify the cracking reactions and cause overcracking of gasoline, thus decreasing gasoline yield. The results clearly demonstrate the superiority of active matrix-based catalysts. At equal zeolite content, the active matrix-based catalysts have a higher gasoline yield than the inactive matrix-based catalysts. The highest gasoline yield was observed on the catalyst with the 20 wt% boehmite nanoparticles ($NC_{30}B_{20}$), which is about 42%.

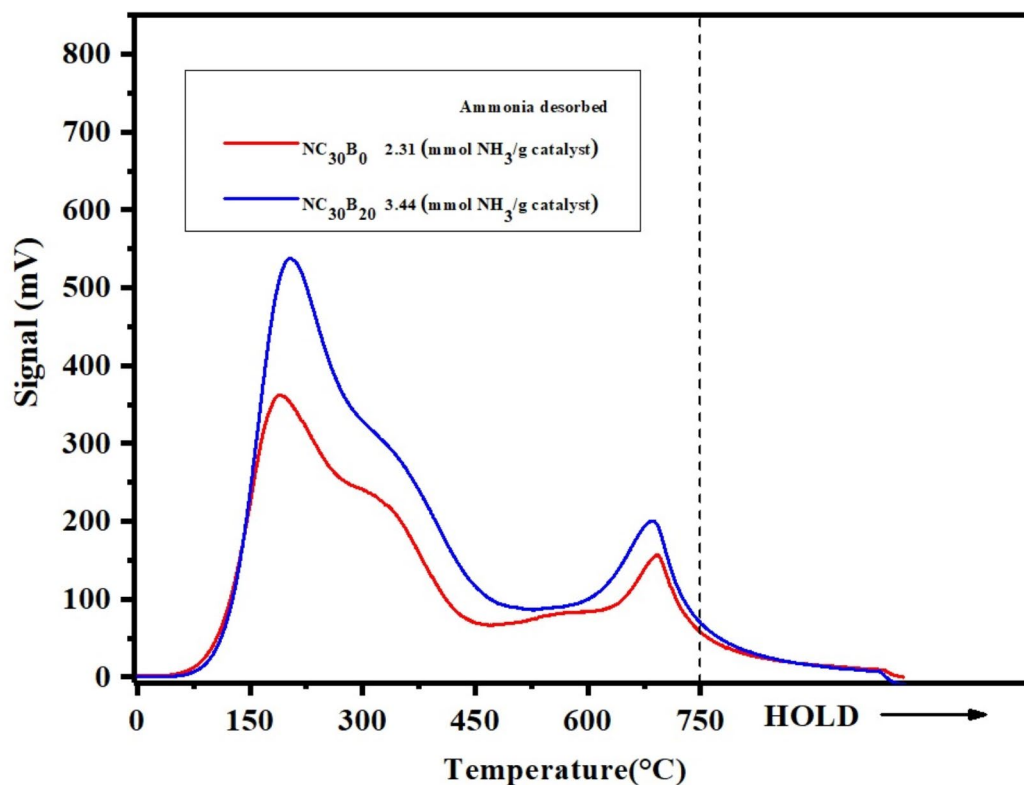


Fig. 11. NH_3 -TPD diagram of the prepared catalysts.

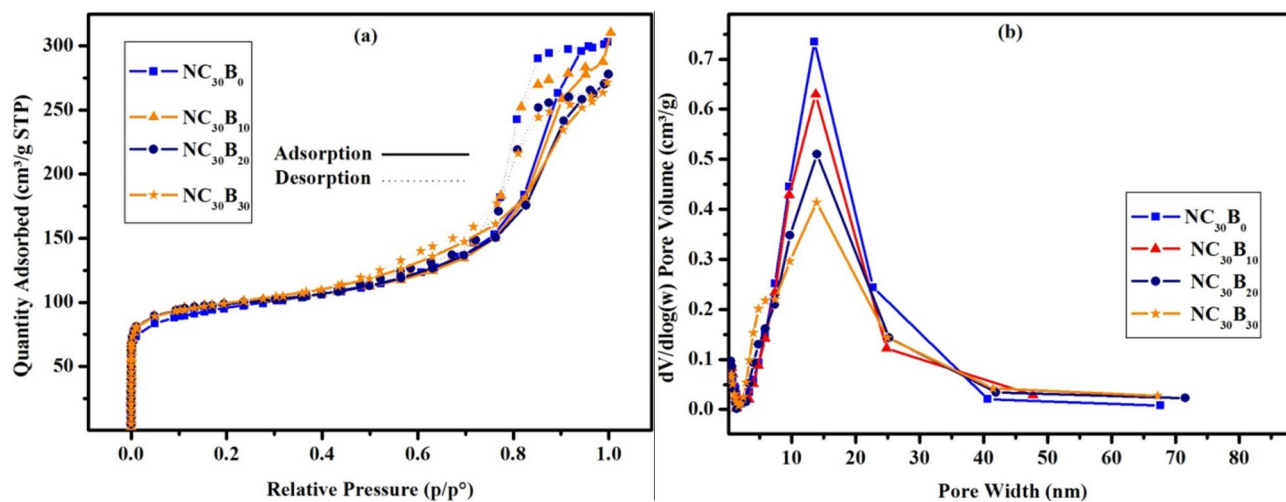


Fig. 12. N_2 adsorption/desorption isotherms (a) and pore size distributions (b) of the prepared catalysts.

Sample	Surface area (m^2/g)	Pore volume (cm^3/g)	Average Pore size (nm)
NC_{30}B_0	346	0.47	5.4
$\text{NC}_{30}\text{B}_{10}$	370	0.44	4.8
$\text{NC}_{30}\text{B}_{20}$	370	0.43	4.6
$\text{NC}_{30}\text{B}_{30}$	359	0.42	4.7

Table 3. Structural properties of the (a) NC_{30}B_0 , (b) $\text{NC}_{30}\text{B}_{10}$, (c) $\text{NC}_{30}\text{B}_{20}$ and $\text{NC}_{30}\text{B}_{30}$ catalysts.

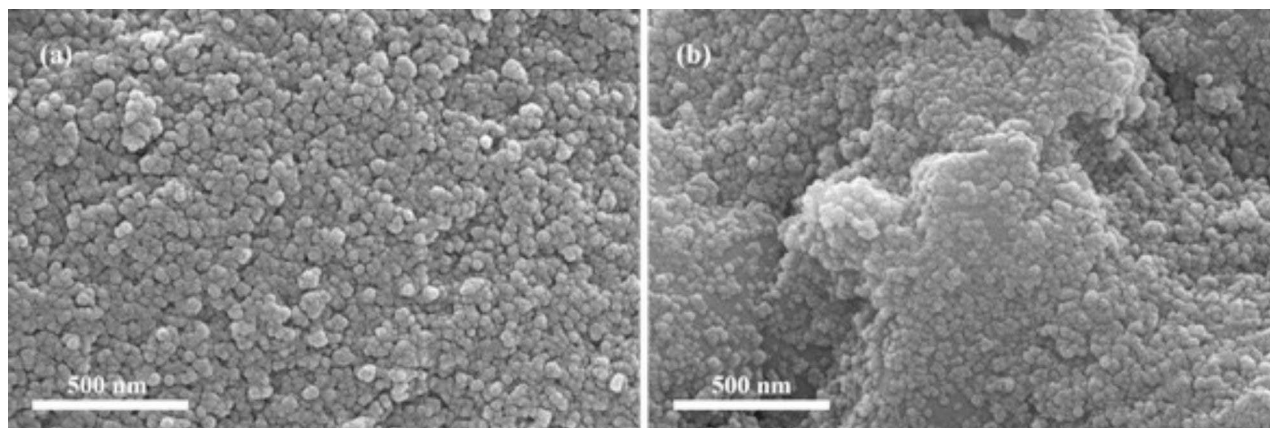


Fig. 13. SEM images of the (a) NC_{30}B_0 and (b) $\text{NC}_{30}\text{B}_{20}$ Catalysts.

The gasoline selectivity is defined as the gasoline yield to conversion ratio, which is one of the most important parameters to evaluate the performance of an RFCC catalyst. Figure 14c illustrates the relationship between the gasoline selectivity and the boehmite content of different prepared catalysts. The increasing catalyst boehmite content increases the gasoline selectivity, which then reaches a constant value and eventually decreases. In fact, the addition of mesoporous boehmite nanoparticles as an active matrix to the catalyst composition causes selective and controlled precracking of heavy hydrocarbon molecules, and by directing the cracked heavy molecules toward the zeolite micropore, gasoline selectivity increases. So, the active matrix-based catalysts have higher gasoline selectivity than the inactive matrix-based catalyst, and the catalyst with the 20 wt% boehmite nanoparticle ($\text{NC}_{30}\text{B}_{20}$) has the highest gasoline selectivity, which is about 65.1%. However, further increasing the boehmite content increases the catalyst acidity, causes overcracking of hydrocarbon molecules, and consequently decreases the gasoline selectivity.

The LCO fraction is the favorable product of the RFCC unit. The LCO yield increases with the catalyst boehmite content and decreases when it reaches a maximum value. In fact, the large hydrocarbon molecules cannot enter the small pores of the zeolite, so the cracking of large hydrocarbon molecules on the mesoporous acidic site of the alumina active matrix and the external surface of the zeolite nanoparticle results in LCO. Hence, the active matrix-based catalyst that has a higher mesoporous active site than the inactive matrix-based catalyst shows higher cracking of large molecules and LCO yield. Also, due to the high frequency of large hydrocarbon molecules with low conversion, the LCO yield increases by increasing the boehmite content and conversion. However, further increases in boehmite content and conversion decrease the amount of these large molecules; thus, LCO yield drops after a maximum value. As can be seen, the catalyst with 20 wt% boehmite nanoparticles ($\text{NC}_{30}\text{B}_{20}$) has the highest LCO yield, which is about 20%.

The HCO fraction is the unfavorable product of the RFCC process, which includes sulfur and aromatic components that should be reduced to the lowest content. As can be seen, HCO yield decreases with rising boehmite content, due to the increase in acidity and the number of catalytic cracking active sites in the mesoporous alumina active matrix. However, the active matrix-based catalysts show a lower HCO yield than the inactive matrix-based catalysts.

Figure 15 displays the influence of the catalyst boehmite content on the coke formation. Coke is the undesired product of the RFCC unit, the formation of which should be kept as low as possible. The obtained results illustrate that active matrix-based catalysts have the lowest coke yield as compared to inactive matrix-based catalysts. In fact, the large hydrocarbon molecules that cannot enter the micropores of the zeolite can cause the blocking of these pores and lead to coke formation. The addition of the alumina active matrix with the mesoporous structure to the catalyst composition, in which heavy hydrocarbons can enter and crack into lighter molecules, does not cause the blockage of the micropores in zeolite. Consequently, the coke yield decreases with the synergetic effect of boehmite and zeolite nanoparticles.

As it can be seen, the synthesized $\text{NC}_{30}\text{B}_{20}$ catalyst with 20 wt% mesoporous boehmite nanoparticles as the active matrix and 30 wt% zeolite nanoparticles balanced with silica showed the best gasoline yield, gasoline selectivity, and LCO yield in the RFCC process. Hence, the catalytic performance of the synthesized $\text{NC}_{30}\text{B}_{20}$ catalyst was compared with the HGY series commercial catalyst of Sinopec Catalyst Company, and the results are presented in Table 4.

According to the results in Table 4, the synthesized $\text{NC}_{30}\text{B}_{20}$ catalyst shows higher values for surface area, total pore volume, and average pore size than the commercial catalyst. In fact, the mesoporous boehmite nanoparticles produce mesopore structure and increase the pore volume and pore size of the synthesized catalyst. Also, the use of zeolite nanoparticles increases the surface area of the synthesized catalyst compared to the commercial catalyst. The NH_3 -TPD analysis showed approximately equal ammonia desorbed from the synthesized and commercial catalysts, which represents the same acidic strength. The catalysts also show approximately equal MAT conversion. As can be seen, the microactivity tests demonstrate that the synthesized $\text{NC}_{30}\text{B}_{20}$ catalyst has a higher desirable product yield, such as gasoline and LCO, a higher gasoline selectivity, and

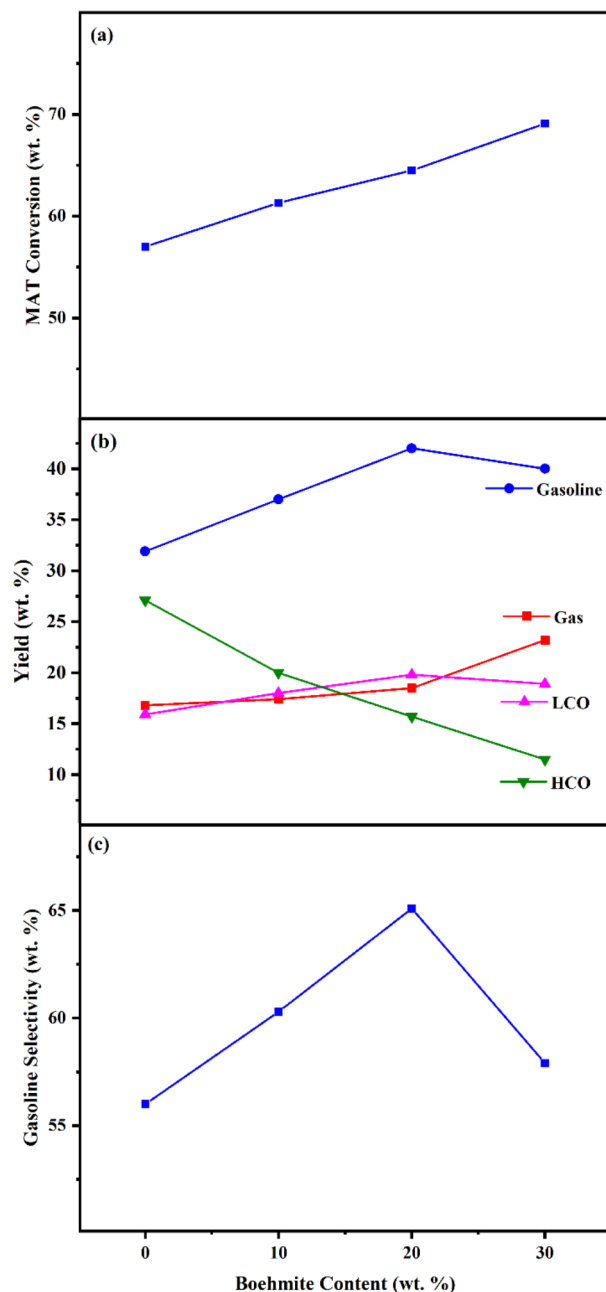


Fig. 14. Correlation of (a) MAT conversion (wt%), (b) product yield (wt%), and (c) gasoline selectivity (wt%) with the boehmite content of different prepared catalysts.

a lower undesirable product yield, such as HCO and gas, than the commercial catalyst in equal MAT conversion. In fact, the optimum catalytic performance of the synthesized $\text{NC}_{30}\text{B}_{20}$ catalyst is related to the synergetic effect of the mesoporous alumina active matrix and zeolite nanoparticles, which leads to a larger pore size, a higher pore volume, and a higher surface area of the catalyst. Therefore, enlarging the pore size of the active matrix and improving the pore distribution of catalysts are the main reasons for the lower molecular diffusion resistance and higher heavy hydrocarbon molecular accessibility of the synthesized catalyst compared to the commercial catalyst, which result in better catalytic performance.

Conclusions

In this work, the boehmite nanoparticles (20–40 nm) and the NaY nanozeolite (20–30 nm) were synthesized and characterized. The XRD analyses clearly demonstrated the formation of boehmite and NaY zeolites with high crystallinity. The BET analysis showed that the prepared boehmite has a mesoporous structure with a surface

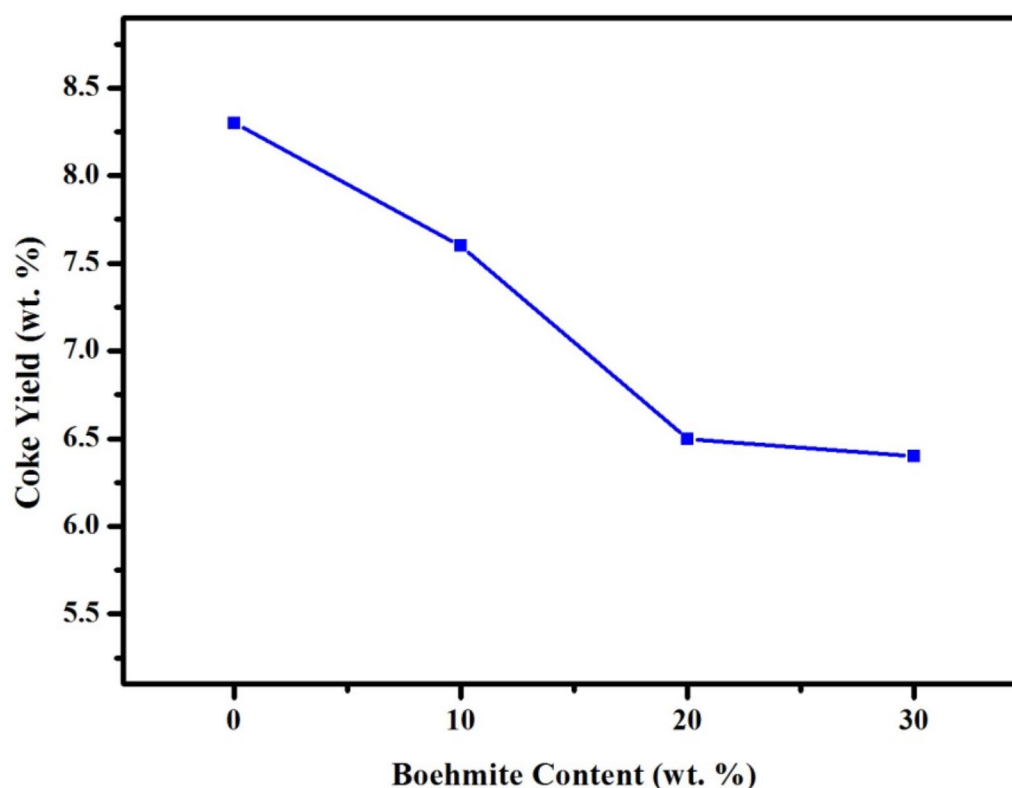


Fig. 15. Correlation of coke yield with the boehmite content of different prepared catalysts.

Item	Synthesized $\text{NC}_{30}\text{B}_{20}$ Catalyst	Commercial Catalyst
Surface area (m^2/g)	370	312
Pore volume (cm^3/g)	0.43	0.18
Average pore size (nm)	4.6	2.3
NH_3 desorbed (mmol /g catalyst)	3.4	3.5
MAT Conversion (wt%)	64.5	64.2
Gas Yield (wt%)	18.5	19.0
Gasoline Yield (wt%)	42.0	38.7
Gasoline Selectivity	65.1	60.3
LCO Yield (wt%)	19.8	18.1
HCO Yield (wt%)	15.7	17.7
Coke Yield (wt%)	6.5	6.5

Table 4. Structural properties and catalytic performance results of the synthesized $\text{NC}_{30}\text{B}_{20}$ and commercial RFCC catalysts.

area of $350 \text{ m}^2/\text{g}$, which is an important parameter in the performance of the active matrix in RFCC catalysts. Afterward, some catalysts were prepared using the mesoporous boehmite nanoparticle as the active matrix and the Y zeolite nanoparticle as the main active component in order to evaluate the synergistic effect of the mesoporous active matrix and the Y zeolite nanoparticles on the catalytic performance. The NH_3 -TPD analysis demonstrated that the acidity improved with the addition of boehmite nanoparticles to the catalyst composition. On the other hand, in equal zeolite content, the active matrix-based catalyst has higher acidity ($\text{NC}_{30}\text{B}_{20}$, $3.44 \text{ mmol NH}_3/\text{g catalyst}$) than the inactive matrix-based catalyst (NC_{30}B_0 , $2.31 \text{ mmol NH}_3/\text{g catalyst}$).

However, in order to evaluate the effect of mesoporous boehmite content on the catalytic performance of the RFCC catalyst, a cracking reaction was carried out using the RFCC unit feedstock of Arak Oil Refinery

Company over the prepared catalysts. The microactivity tests (MAT) demonstrated that, with equal zeolite content, the active matrix-based catalysts have a higher conversion, a higher desirable product yield such as gasoline and LCO, a higher gasoline selectivity, and lower undesirable product yield such as HCO and coke than the inactive matrix-based catalyst. In fact, the optimum catalytic performance of the active matrix-based catalysts is related to the mesoporous active site and the higher acidity of the alumina active matrix, which leads to lower molecular diffusion resistance and higher heavy hydrocarbon molecular accessibility. Moreover, the active matrix-based catalyst ($\text{NC}_{30}\text{B}_{20}$) with a BET area of $370 \text{ m}^2/\text{g}$ showed the best catalytic performance in the RFCC process. The synthesized $\text{NC}_{30}\text{B}_{20}$ catalyst with 20 wt% mesoporous boehmite nanoparticles as the active matrix and 30 wt% zeolite nanoparticles balanced with silica had the highest gasoline yield (42 wt%) and gasoline selectivity (65.1 wt%). The catalytic performance test results showed that in equal MAT conversion (almost 64 wt%), the synthesized $\text{NC}_{30}\text{B}_{20}$ catalyst has higher desirable product yields, such as gasoline (42.0 wt% synthesized catalyst versus 38.7 wt% commercial catalyst) and LCO (19.8 wt% synthesized catalyst versus 18.1 wt% commercial catalyst), higher gasoline selectivity (65.1 wt% synthesized catalyst versus 60.3 wt% commercial catalyst), and lower undesirable product yields such as HCO (15.7 wt% synthesized catalyst versus 17.7 wt% commercial catalyst) and gas (18.5 wt% synthesized catalyst versus 19.0 wt% commercial catalyst) than the commercial catalyst. In fact, the better catalytic performance of the synthesized $\text{NC}_{30}\text{B}_{20}$ catalyst is attributed to the synergetic effect of the mesoporous alumina active matrix and zeolite nanoparticles, which leads to a larger pore size, a higher pore volume, and a higher surface area of the catalyst. Therefore, lower molecular diffusion resistance and higher heavy hydrocarbon molecular accessibility are the main reasons for the superiority of the synthesized catalyst over the commercial catalyst.

Data availability

All data generated or analyzed during this study are included in this published article.

Received: 23 August 2024; Accepted: 6 January 2025

Published online: 13 January 2025

References

- Mahgoub, K. A. & Al-Khattaf, S. Catalytic cracking of hydrocarbons in a riser simulator: the effect of catalyst accessibility and acidity. *Energy Fuels*. **19**, 329–338. <https://doi.org/10.1021/ef049848p> (2005).
- Sadeghbeigi, R. *Fluid Catalytic Cracking Handbook: An Expert Guide to the Practical Operation, Design, and Optimization of FCC Units* third edn (Elsevier, 2012).
- Jones, D. S. & Pujado, P. R. *Handbook of Petroleum Processing* (Springer Science & Business Media, 2006).
- Pan, M. et al. Construction and practical application of a novel zeolite catalyst for hierarchically cracking of heavy oil. *J. Catal.* **369**, 72–85. <https://doi.org/10.1016/j.jcat.2018.10.032> (2019).
- Gary, J. H., Handwerk, G. E. & Kaiser, M. J. *Petroleum Refining: Technology and Economics* (fifth ed., CRC, 2007).
- Speight, J. G. *The Chemistry and Technology of Petroleum* (fifth ed., CRC, 2014).
- Brueva, T. R., Mishin, I. V. & Kapustin, G. I. Distribution of acid-site strengths in hydrogen zeolites and relationship between acidity and catalytic activity. *Thermochim. Acta*. **379**, 15–23. [https://doi.org/10.1016/S0040-6031\(01\)00597-4](https://doi.org/10.1016/S0040-6031(01)00597-4) (2001).
- Haag, W. O., Lago, R. M. & Weisz, P. B. The active site of acidic aluminosilicate catalysts. *Nature* **309**, 589–591. <https://doi.org/10.1038/309589a0> (1984).
- Pujro, R., Falco, M. & Sedran, U. Catalytic Cracking of Heavy Aromatics and Polycyclic Aromatic Hydrocarbons over Fluidized Catalytic cracking catalysts. *Energy Fuels*. **29**, 1543–1549. <https://doi.org/10.1021/ef502707w> (2015).
- Venuto, P. B. & Habib, E. T. Jr *Fluid Catalytic Cracking with Zeolite Catalysts* (Marcel Dekker, 1979).
- Liu, P. et al. Vanadium contamination on the stability of zeolite USY and efficient passivation by La_2O_3 for cracking of residue oil. *Microporous Mesoporous Mater.* **279**, 345–351. <https://doi.org/10.1016/j.micromeso.2019.01.023> (2019).
- Ihli, J. et al. A three-dimensional view of structural changes caused by deactivation of fluid catalytic cracking catalysts. *Nat. Commun.* **8**, 809. <https://doi.org/10.1038/s41467-017-00789-w> (2017).
- Aghaei, E., Karimzadeh, R., Godini, H. R., Gurlo, A. & Gorke, O. Improving the physicochemical properties of Y zeolite for catalytic cracking of heavy oil via sequential steam-alkali-acid treatments. *Microporous Mesoporous Mater.* **294**, 109854. <https://doi.org/10.1016/j.micromeso.2019.109854> (2020).
- Al-Shammari, A. A. et al. Catalytic cracking of heavy naphtha-range hydrocarbons over different zeolites structures. *Fuel Process. Technol.* **122**, 12–22. <https://doi.org/10.1016/j.fuproc.2014.01.021> (2014).
- Liu, X. et al. A diffusion anisotropy descriptor links morphology effects of H-ZSM-5 zeolites to their catalytic cracking performance. *Commun. Chem.* **4**, 107. <https://doi.org/10.1038/s42004-021-00543-w> (2021).
- Zhao, R. et al. Promotion of adsorptive and catalytic properties of zeolitic Brønsted acid sites by proximal extra-framework $\text{Si}(\text{OH})_x$ groups. *Nat. Catal.* **6**, 68–79. <https://doi.org/10.1038/s41929-022-00906-z> (2023).
- Bhatia, S. *Zeolite Catalysts: Principles and Applications* (CRC, 1989).
- Barthomeuf, D. Basic zeolites: characterization and uses in adsorption and catalysis. *Cat. Rev. Sci. Eng.* **38**, 521–612. <https://doi.org/10.1080/01614949608006465> (1996).
- Weitkamp, J., Weiß, U. & Ernst, S. New aspects and trends in zeolite catalysis. *Stud. Surf. Sci. Catal.* **94**, 363–380. [https://doi.org/10.1016/S0167-2991\(06\)81244-9](https://doi.org/10.1016/S0167-2991(06)81244-9) (1995).
- Smirniotis, P. G., Davydov, L. & Ruckenstein, E. Composite zeolite-based catalysts and sorbents. *Cat. Rev. Sci. Eng.* **41**, 43–113. <https://doi.org/10.1081/CR-100101949> (1999).
- Gackowski, M. et al. Hierarchical zeolites Y obtained by desilication: porosity, acidity and catalytic properties. *Microporous Mesoporous Mater.* **263**, 282–288 (2018).
- Awala, H. et al. Template-free nanosized faujasite-type zeolites. *Nat. Mater.* **14**, 447–451. <https://doi.org/10.1038/nmat4173> (2015).
- Sonthisawate, T. et al. Catalytic cracking reaction of vacuum gas oil and atmospheric residue by zeolite-containing microporous and mesoporous composites using curie point pyrolyzer. *Fuel Process. Technol.* **142**, 337–344 (2016). <https://doi.org/10.1016/j.fuproc.2015.10.016>
- Karger, J. & Ruthven, D. M. *Diffusion in Zeolites and Other Microporous Solids* (Wiley, 1992).
- Ishihara, A. Preparation and reactivity of hierarchical catalysts in catalytic cracking. *Fuel Process. Technol.* **194**, 106–116. <https://doi.org/10.1016/j.fuproc.2019.05.039> (2019).
- Tosheva, L. & Valtchev, V. P. Nanozeolites: synthesis, crystallization mechanism, and applications. *Chem. Mater.* **17**, 2494–2513. <https://doi.org/10.1021/cm047908z> (2005).

27. Corma, A. From microporous to mesoporous molecular sieve materials and their use in catalysis. *Chem. Rev.* **97**, 2373–2420. <https://doi.org/10.1021/cr960406n> (1997).
28. Breck, D. W. *Zeolite Molecular Sieves: Structure, Chemistry and Use* (Wiley, 1973).
29. Baerlocher, C., McCusker, L. B. & Olson, D. H. *Atlas of Zeolite Framework Types, Sixth ed* (Elsevier, 2007).
30. Kubicek, N. et al. Stabilization of zeolite beta for FCC application by embedding in amorphous matrix. *Appl. Catal. Gen.* **175**, 159–171. [https://doi.org/10.1016/S0926-860X\(98\)00207-5](https://doi.org/10.1016/S0926-860X(98)00207-5) (1998).
31. Falco, M., Morgado, E., Amadeo, N. & Sedran, U. Accessibility in alumina matrices of FCC catalysts. *Appl. Catal. Gen.* **315**, 29–34. <https://doi.org/10.1016/j.apcata.2006.08.028> (2006).
32. Wojciechowski, B. W. & Corma, A. *Catalytic Cracking: Catalysts, Chemistry, and Kinetics* (Marcel Dekker, 1986).
33. Ghojavand, S. et al. Interplay between alkali-metal cations and silanol sites in nanosized CHA zeolite and implications for CO₂ adsorption. *Commun. Chem.* **6**, 134. <https://doi.org/10.1038/s42004-023-00918-1> (2023).
34. Vuong, G. T., Hoang, V. T., Nguyen, D. T. & Do, T. O. Synthesis of nanozeolite and nanozeolite-based FCC catalyst, and their catalytic activity in gas oil cracking reaction. *Appl. Catal. A: Gen.* **382**, 231–239. <https://doi.org/10.1016/j.apcata.2010.04.049> (2010).
35. Rajagopalan, K., Peters, A. W. & Edwards, G. C. Influence of zeolite particle size on selectivity during fluid catalytic cracking. *Appl. Catal.* **23**, 69–80. [https://doi.org/10.1016/S0166-9834\(00\)81453-0](https://doi.org/10.1016/S0166-9834(00)81453-0) (1986).
36. Shojaei, S. et al. Application of Taguchi method and response surface methodology into the removal of malachite green and auramine-O by NaX nanozeolites. *Sci. Rep.* **11**, 16054. <https://doi.org/10.1038/s41598-021-95649-5> (2021).
37. Rase, H. F. *Handbook of Commercial Catalysts: Heterogeneous Catalysts* (CRC Press LLC, 2000).
38. Sadeghbeigi, R. *Fluid Catalytic Cracking Handbook: Design Operation and Troubleshooting of FCC Facilities* second edn (Gulf Publishing Company, 2000).
39. Al-Khattaf, S. The influence of alumina on the performance of FCC catalysts during hydrotreated VGO catalytic cracking. *Energy Fuels*. **17**, 62–68. <https://doi.org/10.1021/ef020066a> (2003).
40. Moradi, P., Kikhavani, T. & Abbasi Tyula, Y. A new samarium complex of 1,3-bis (pyridin-3-ylmethyl) thiourea on boehmite nanoparticles as a practical and recyclable nanocatalyst for the selective synthesis of tetrazoles. *Sci. Rep.* **13**, 5902. <https://doi.org/10.1038/s41598-023-33109-y> (2023).
41. Zheng, Y., Song, J. & Xu, X. Peptization mechanism of boehmite and its effect on the preparation of a fluid catalytic cracking catalyst. *Ind. Eng. Chem. Res.* **53**, 10029–10034. <https://doi.org/10.1021/ie501060g> (2014).
42. Barclay, D. A. Process for producing high porosity boehmite aluminas. *US Pat.*, **US20080193369** (2008).
43. Wang, B. et al. Studies on the preliminary cracking: the reasons why matrix catalytic function is indispensable for the catalytic cracking of feed with large molecular size. *J. Ene Chem.* **25**, 641–653. <https://doi.org/10.1016/j.jechem.2016.02.014> (2016).
44. Woltermann, G. M., Magee, J. S. & Griffith, S. D. Commercial preparation and characterization of FCC catalysts. *Stud. Surf. Sci. Catal.* **76**, 105–144. [https://doi.org/10.1016/S0167-2991\(08\)63827-6](https://doi.org/10.1016/S0167-2991(08)63827-6) (1993).
45. Otterstedt, J. E., Zhu, Y. M. & Sterte, J. Catalytic cracking of heavy oil over catalysts containing different type of zeolite Y in active and inactive matrices. *Appl. Catal.* **38**, 143–155. [https://doi.org/10.1016/S0166-9834\(00\)80993-8](https://doi.org/10.1016/S0166-9834(00)80993-8) (1998).
46. Liu, J. et al. Hierarchical macro-meso-microporous ZSM-5 Zeolite Hollow fibers with highly efficient Catalytic cracking capability. *Sci. Rep.* **4**, 7276. <https://doi.org/10.1038/srep07276> (2014).
47. Ahmad, A. et al. Synthesis, characterization and catalytic testing of MCM-22 derived catalysts for n-hexane cracking. *Sci. Rep.* **11**, 9176. <https://doi.org/10.1038/s41598-021-88093-y> (2021).
48. Amini, E., Ahmadi, K., Rashidi, A., Youzbashi, A. & Rezaei, M. Preparation of nanozeolite-based RFCC catalysts and evaluation of their catalytic performance in RFCC process. *J. Taiwan Inst. Chem. Eng.* **100**, 37–46. <https://doi.org/10.1016/j.jtice.2019.04.027> (2019).
49. Tsukada, T. & Nakamura, H. Pseudoboehmite powder for catalyst carrier and process for preparing the same. *US Pat.*, 6174511 (2001).
50. Lu, C. L. et al. Crystalline nanotubes of γ -AlOOH and γ -Al₂O₃: hydrothermal synthesis, formation mechanism and catalytic performance. *Nanotechnology* **20**, 1–9. <https://doi.org/10.1088/0957-4484/20/21/215604> (2009).
51. Morales-Pacheco, P., Alvarez, F., Bucio, L. & Domínguez, J. M. Synthesis and structural properties of zeolitic nanocrystals II: FAU-type zeolites. *J. Phys. Chem. C*. **113**, 2247–2255. <https://doi.org/10.1021/jp8070713> (2009).
52. Coudurier, G., Naccache, C. & Vedrine, J. C. Uses of IR spectroscopy in identifying ZSM zeolite structure. *J. Chem. Soc. Chem. Commun.* **24**, 1413–1415. <https://doi.org/10.1039/c39820001413> (1982).
53. Holmberg, B. A., Wang, H., Norbeck, J. M. & Yan, Y. Controlling size and yield of zeolite Y nanocrystals using tetramethylammonium bromide. *Microporous Mesoporous Mater.* **59**, 13–28. [https://doi.org/10.1016/S1387-1811\(03\)00271-3](https://doi.org/10.1016/S1387-1811(03)00271-3) (2003).
54. Leofanti, G., Padovan, M., Tozzola, G. & Venturelli, B. Surface area and pore texture of catalysts. *Catal. Today*. **41**, 207–219. [https://doi.org/10.1016/S0920-5861\(98\)00050-9](https://doi.org/10.1016/S0920-5861(98)00050-9) (1998).
55. Lónyi, F. & Valyon, J. On the interpretation of the NH₃-TPD patterns of H-ZSM-5 and H-mordenite. *Microporous Mesoporous Mater.* **47**, 293–301. [https://doi.org/10.1016/S1387-1811\(01\)00389-4](https://doi.org/10.1016/S1387-1811(01)00389-4) (2001).
56. Lónyi, F. & Valyon, J. A TPD and IR study of the surface species formed from ammonia on zeolite H-ZSM-5, H-mordenite and H-beta. *Thermochim Acta*. **373**, 53–57. [https://doi.org/10.1016/S0040-6031\(01\)00458-0](https://doi.org/10.1016/S0040-6031(01)00458-0) (2001).
57. Topsoe, N. Y., Pedersen, K. & Derouane, E. G. Infrared and temperature-programmed desorption study of the acidic properties of ZSM-5-type zeolites. *J. Catal.* **70**, 41–52. [https://doi.org/10.1016/0021-9517\(81\)90315-8](https://doi.org/10.1016/0021-9517(81)90315-8) (1981).
58. Hidalgo, C. V., Itoh, H., Hattori, T., Niwa, M. & Murakami, Y. Measurement of the acidity of various zeolites by temperature-programmed desorption of ammonia. *J. Catal.* **85**, 362–369. [https://doi.org/10.1016/0021-9517\(84\)90225-2](https://doi.org/10.1016/0021-9517(84)90225-2) (1984).
59. Tonetto, G., Atlas, J. & De Lasa, H. FCC catalysts with different zeolite crystallite sizes: acidity, structural and reactivity. *Appl. Catal. A: Gen.* **270**, 9–25. <https://doi.org/10.1016/j.apcata.2004.03.042> (2004).
60. Hosseinpour, N., Mortazavi, Y., Bazary, A. & Khodadadi, A. A. Synergetic effects of Y-zeolite and amorphous silica-alumina as main FCC catalyst components on triisopropylbenzene cracking and coke formation. *Fuel Process. Technol.* **90**, 171–179. <https://doi.org/10.1016/j.fuproc.2008.08.013> (2009).

Acknowledgements

The authors gratefully acknowledge the supports from Material and Energy Research Center by Grant No. 481394052.

Author contributions

E.A., A.R., and M.R. devised the main conceptual ideas and developed the theory. E.A., K.A., and A.A.Y. conceived and planned the experiments, sample preparation, and analyses. E.A. and S.M. carried out the experiments, contributed to sample preparation, and conducted analyses. K.A. and A.R. supervised the project. E.A. and S.M. wrote the main manuscript text. All authors contributed to the interpretation of the results and reviewed the manuscript.

Declarations

Competing interests

The authors declare no competing interests.

Additional information

Correspondence and requests for materials should be addressed to E.A. or A.R.

Reprints and permissions information is available at www.nature.com/reprints.

Publisher's note Springer Nature remains neutral with regard to jurisdictional claims in published maps and institutional affiliations.

Open Access This article is licensed under a Creative Commons Attribution-NonCommercial-NoDerivatives 4.0 International License, which permits any non-commercial use, sharing, distribution and reproduction in any medium or format, as long as you give appropriate credit to the original author(s) and the source, provide a link to the Creative Commons licence, and indicate if you modified the licensed material. You do not have permission under this licence to share adapted material derived from this article or parts of it. The images or other third party material in this article are included in the article's Creative Commons licence, unless indicated otherwise in a credit line to the material. If material is not included in the article's Creative Commons licence and your intended use is not permitted by statutory regulation or exceeds the permitted use, you will need to obtain permission directly from the copyright holder. To view a copy of this licence, visit <http://creativecommons.org/licenses/by-nc-nd/4.0/>.

© The Author(s) 2025